

TV Mon - post mass transfer Algol type binary with δ Scuti pulsations in primary component.

Mikhail Kovalev,^{1,2,3*} Zhenwei Li,^{1,2} Jianping Xiong,^{1,2} Azizbek Matekov,^{1,2} Zhang Bo,⁴ Xuefei Chen^{1,2,5} and Zhanwen Han^{1,2,5}

¹Yunnan Observatories, China Academy of Sciences, Kunming 650216, China

²Key Laboratory for the Structure and Evolution of Celestial Objects, Chinese Academy of Sciences, Kunming 650011, China

³International Centre of Supernovae, Yunnan Key Laboratory, Kunming 650216, China

⁴Key Laboratory of Optical Astronomy, National Astronomical Observatories, Chinese Academy of Sciences, Beijing 100101, China

⁵Center for Astronomical Mega-Science, Chinese Academy of Sciences, 20A Datun Road, Chaoyang District, Beijing 100012, China

Accepted XXX. Received YYY; in original form ZZZ

ABSTRACT

We present a study of the detached eclipsing binary TV Mon using spectra from the LAMOST medium-resolution survey and ASAS-SN, CoRoT photometry. We applied multiple-epochs spectral fitting to derive RV and spectral parameters. The analysis of eclipses in CoRoT data told us relative sizes of the stellar components and almost edge-on circular orbit. Combining spectral and photometrical solution we estimated masses and radii of the components: $M_{A,B} = 2.063 \pm 0.033, 0.218 \pm 0.004 M_{\odot}$, $R_{A,B} = 2.427 \pm 0.014, 2.901 \pm 0.016 R_{\odot}$. SED analysis and Gaia parallax allowed us to get estimation of temperatures $T_{\text{eff},A,B} = 7624^{+194}_{-174}, 5184^{+130}_{-123}$ K and distance $d = 907 \pm 11$ pc. We identified three δ Scuti type pulsation frequencies in primary component, while we also suspect TV Mon having a long period variability with period $P_{\text{long}} \sim 128$ days and spot activity in secondary component. This system experienced intensive mass transfer and mass ratio reversal in the past, currently showing no signs of mass transfer in the spectra. The low mass component will lose its outer envelope and shrink to the helium white dwarf, which mass and orbital period are in good agreement with evolutionary models predictions.

Key words: stars : fundamental parameters – binaries : eclipsing – binaries : spectroscopic – stars individual: TV Mon

1 INTRODUCTION

Detached eclipsing binaries (dEBs) are very important astronomical objects, which allow us to study stellar structure and evolution (Torres et al. 2010; Han et al. 2020). Many close eclipsing binaries have significantly different masses of the components, which indicates there was mass-transfer in the past (Chen et al. 2020). Quite often high-frequency pulsations can be found in these systems using precise space-based photometry (Chen et al. 2021; Wang et al. 2023). Recently Xiong et al. (2023) derived masses and radii for 56 dEBs by using the LAMOST (Large Sky Area Multi-Object fiber Spectroscopic Telescope, also known as Guoshoujing telescope) medium-resolution survey (MRS) spectra and ground-based time-domain photometry. We select one of these stars: TV Mon with large mass ratio to analyse it using precise space-based photometry and multiple-epoch spectra fitting, developed in Kovalev et al. (2022a, 2023).

The paper is organised as follows: in Sections 2 and 3 we describe the observations and methods. Section 4 presents our results. In Section 7 we discuss the results in context of binary system evolution. In Section 8 we summarise the paper and draw conclusions.

2 OBSERVATIONS

2.1 Spectra

LAMOST is a 4-meter quasi-meridian reflective Schmidt telescope with 4000 fibers installed on its 5° field of view focal plane. These configurations allow it to observe spectra for at most 4000 celestial objects simultaneously (Cui et al. (2012); Zhao et al. (2012)). All available spectra were downloaded from www.lamost.org/dr9/ under the designation J062822.72+051257.2. We use the spectra taken at a resolving power of $R = \lambda/\Delta\lambda \sim 7500$. Each spectrum is divided into two arms: blue from 4950 Å to 5350 Å and red from 6300 Å to 6800 Å. We convert the heliocentric wavelength scale in the observed spectra from vacuum to air using PYASTRONOMY

* E-mail: mikhail.kovalev@ynao.ac.cn

(Czesla et al. 2019) and apply zero point correction using values from Zhang et al. (2021), when it is possible. Observations are carried out from 2019-02-16 till 2020-03-05, covering 12 nights with time base of 373 days. The period is short ($P = 4.179742$ d Kreiner (2004)) therefore we analysed spectra taken during short 20 minutes exposures, unlike Kovalev et al. (2022a,b), where spectra stacked for the whole night were used. In total we have 35 spectra, where the average signal-to-noise ratio (S/N) of a spectrum ranges from 9 to 60 pix^{-1} for blue arm and from 10 to 82 pix^{-1} for red arm of the spectrum, with the majority of the spectra have S/N around 40 pix^{-1} .

2.2 Photometry

We have downloaded publicly available V band light curve (LC) from the ASAS-SN portal¹. It contains only 168 datapoints and covers timebase 1443 days.

The CoRoT (Convection, Rotation and planetary Transit) satellite mission (Barge et al. 2008) provides very high-quality LC. We download it² and use systematic-corrected “WHITEFLUXSYS” data, with “STATUS” field equals to zero (3443 datapoints in total, time coverage of ~ 32 days). We normalise this dataset by dividing it by median values in the out-of-eclipse regions of the two time intervals: $\text{BJD} < 2454753.5$ days (it has exposure time 512^s) and $\text{BJD} > 2454753.5$ days (it has exposure time 32^s). The phase-folded LC shows two eclipses with short, flat minima (~ 40 min), while many small gaps and high-frequency pulsations are clearly visible, see Figure 1. These gaps are artefacts of removal of the “jumps”, caused by the cosmic radiation, which mostly occurred when the satellite cross the South Atlantic Anomaly (SAA) (Auvergne et al. 2009; Sokolovsky et al. 2010).

Timeseries from WISE satellite (Cutri et al. 2013) are available for this system in $W1$ and $W2$ filters, see Appendix B. In infrared light secondary eclipse is much deeper, than in visual, which indicates a larger contribution of secondary to the total light of the system in this regime. However these LC contains only 78 datapoints and limb darkening coefficients are unavailable for these filters, so we don’t use these data for LC analysis.

Unfortunately Transiting Exoplanet Survey Satellite (TESS Ricker et al. 2015) mission did not observe this system, because it is located close to the ecliptic plane, exactly in the gap between two sectors of observations.

3 METHODS

3.1 Spectral fitting

Our spectroscopic analysis includes two consecutive stages:

(i) analysis of individual observations by binary and single-star spectral models, where we normalise the spectra and make a rough estimation of the spectral parameters, see brief description in Section 3.1.1.

(ii) simultaneous fitting of multiple-epochs with a binary spectral model, using constraints from binary dynamics and values from the previous stage as an input, see Section 3.1.2.

3.1.1 Individual spectra.

The single-star spectral model is same as in Kovalev et al. (2024) and described in Appendix A. The normalised binary model spectrum is generated as a sum of the two Doppler-shifted, normalised single-star model spectra $f_{\lambda,i}$ scaled according to the difference in luminosity, which is a function of the T_{eff} and stellar size. We use following equation:

$$f_{\lambda,\text{binary}} = \frac{f_{\lambda,2} + k_{\lambda} f_{\lambda,1}}{1 + k_{\lambda}}, \quad k_{\lambda} = \frac{B_{\lambda}(T_{\text{eff},1})}{B_{\lambda}(T_{\text{eff},2})} k_R, \quad (1)$$

where k_{λ} is the luminosity ratio per wavelength unit, B_{λ} is the black-body radiation (Planck function), T_{eff} is the effective temperature, k_R - light ratio coefficient. Throughout the paper we always assume the primary star to be brighter.

The binary model spectrum is later multiplied by the normalisation function, which is a linear combination of the first four Chebyshev polynomials (similar to Kovalev et al. 2019), defined separately for blue and red arms of the spectrum. The resulting spectrum is compared with the observed one using the `scipy.optimize.curve_fit` function, which provides optimal spectral parameters, radial velocities (RV) of each component plus the light ratio and two sets of four coefficients of Chebyshev polynomials. We keep metallicity equal for both components. In total we have 18 free parameters for a binary fit.

3.1.2 Multiple-epochs fitting.

We explore the results from the fitting of the individual epochs and find that a result’s quality clearly depends on separation of RVs. Clear double-lined spectra show that spectral lines are significantly broadened ($V \sin i \sim 30 \text{ km s}^{-1}$), thus Rossiter-McLaughlin (RM) effect (Rossiter 1924; McLaughlin 1924) can be observed during eclipses.

If two components in our binary system are gravitationally bound, their radial velocities should agree with the following equation:

$$\text{RV}_A = \gamma(1 + q) - q\text{RV}_B, \quad (2)$$

where q - mass ratio and γ - systemic velocity. Using this equation we can directly measure the systemic velocity and mass ratio. We should note that this equation is valid in assumption of absence of RM effect, which can be justified by excluding spectral observations during the eclipses, and no difference in gravitational redshifts for two components $\Delta\gamma_i$. Given high mass ratio, we estimate this difference $\Delta\gamma_A - \Delta\gamma_B \sim 0.5 \text{ km s}^{-1}$ using system parameters from Xiong et al. (2023) and Equation 1 from El-Badry (2022), which is comparable to the usual precision of our RV measurements and typical zero point offsets of LAMOST-MRS (Zhang et al. 2021). Thus this effect can be neglected in our analysis.

To reduce the number of free parameters in the multiple-epochs fitting we can select only one component RV for fitting and compute values for another one using Equation 2. We fit previously normalised individual epoch’s spectra, using their binary spectral parameters values for initialisation. We repeat this five times using only manually selected best individual epoch’s fit initialisation. We select the spectroscopic solution with minimal χ^2 as a final result. Surface gravity $\log(g)$ is poorly constrained by the spectra alone, thus we assign it: initially to values from Xiong et al. (2023) and than to the new estimation from LC fit, see Section 3.2. We repeat this iteratively until both spectra and LC were reasonably fitted.

¹ <https://asas-sn.osu.edu/variables/243496>

² available on VizieR <http://cdsarc.u-strasbg.fr/saadavizier/download?oid=1153203439145087791> (COROT Team 2016)

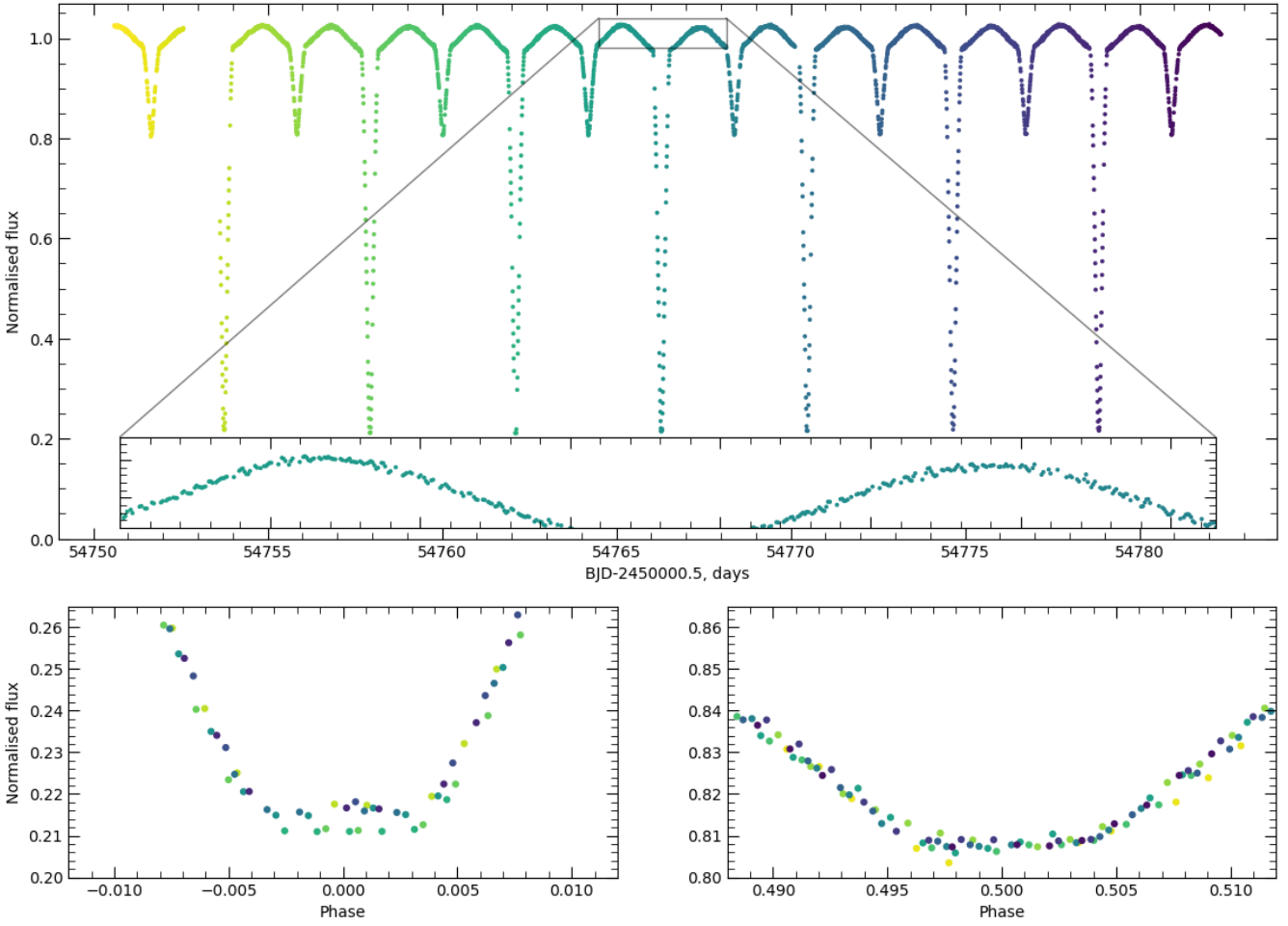


Figure 1. Normalised CoRoT light curve, with inline plot showing gaps and high-frequency pulsations (top panel) and phased eclipses, showing flat regions (bottom panel).

Finally we get new RV measurements for selected component, q , γ and spectral parameters for both component. We can repeat these calculations taking another component's RVs as a fitting parameters, but derived spectral parameters will be swapped and mass/light ratio will be inverted. Agreement between two solutions can validate assumptions of Equation 2. Then we can use these RV measurements of both components in further analysis.

3.2 Light curve fitting

Visual inspection of CoRoT LC tell us that there is a short total eclipse during the main minimum and a transit during the secondary minimum, separated by half of the period. Thus it is reasonable to assume edge-on circular orbit with “central” eclipse (inclination $i = 90^\circ$) and compute approximations for relative radii R_i/a using pure geometry of spherical stars, see Formulae 12,13 from the great book by Tsevevich (1980):

$$R_A/a + R_B/a = \sin \Theta_1, \quad (3)$$

$$R_B/a - R_A/a = \sin \Theta_2, \quad (4)$$

$$2\Theta_1 = D, \quad 2\Theta_2 = D_{\text{tot}}, \quad (5)$$

where D and D_{tot} are durations of eclipse and it's total (flat) part, both divided by period, respectively, a - is a radius of circular orbit.

This gives us $R_{A,B}/a \sim 0.163, 0.190$. These values can be used to initialize detailed LC modelling.

We analyse available LC datasets in two steps using different codes. Originally CoRoT LC and RV data were fitted by JKTEBOP and Transit Light Curve Modeler code (TLCM). These two codes assume spherical shape of the stars and works extremely fast, although unable to fit several LC simultaneously. We use their solutions to check consistency of our data and to derive period, mass ratio and orbital parameters of the system. After this ELLC code was used to simultaneously fit ASAS-SN and CoRoT LCs with fixed period, mass ratio and orbit.

3.2.1 JKTEBOP

We used the JKTEBOP code (version 40)³ by Southworth (2013) to simultaneously fit the LC and RV timeseries. We used quadratic limb darkening coefficients provided by the JKTLD code⁴ and linearly interpolated them for spectral parameters. The eccentricity

³ JKTEBOP is written in FORTRAN77 and the source code is available at <http://www.astro.keele.ac.uk/jkt/codes/jktebop.html>

⁴ it is provided together with JKTEBOP

was set to zero and the systemic velocity was fitted for both binary components. In total we fit for 16 parameters: J the central surface brightness ratio, $(R_A + R_B)/a$ the ratio of the sum of stellar radii to the semimajor axis, R_B/R_A the ratio of the radii, i the inclination, S_0 nuisance parameter for the out-of-eclipse magnitude, reflected light $A_{A,B}$, P the period, t_0 , semiamplitudes and systemic velocities $K_{A,B}$, $\gamma_{A,B}$, and S_0 . We use integration ring size 1° .

At first we run the JKTEBOP code in the mode ‘‘Task 4’’ to discard outliers larger than three sigma (only 26 datapoints were removed from LC dataset, while all 23 RV were kept for both components) and allow it adjusting observational errors through several iterations until reduced χ^2 reaches unity. Then we run JKTEBOP in the Monte Carlo mode (Task 8 ‘‘MC’’) to estimate uncertainties using 10000 simulations.

3.2.2 TLCM

Presence of total eclipse and transit in the CoRoT LC allows us to use TLCM, which was developed and actively used to fit exoplanet transits in CoRoT data (Csizmadia 2020). It allows to use RV data from two components in ‘‘SB2’’ mode and estimate parameters uncertainties using Monte Carlo simulations. Reflection, ellipsoidal and beaming effects are included in modelling for both components. We fix period $P = 4.179741$ day and eccentricity $e = 0$, while fit for all other parameters, including limb darkening coefficients for both stars $u_{+,-}$ and parabolic trend with time. Final solution is determined as a median of 25000 MC simulations with 10 walkers.

3.2.3 ELLC

The ELLC code (Maxted 2016), uses triaxial ellipsoids as component’s shapes, which is better approximation than the sphere, especially when ‘‘roche’’ shape is chosen. In order to save computational time we use only LC data from CoRoT and ASAS-SN without RV and fix $a \sin i$, q , P to the values from TLCM solution. Limb and gravity darkening coefficients were computed using interpolator built-in in ELLC and values of stellar parameters from Table 3. Both LCs were fitted simultaneously with fractional radii $R_{A,B}/a$, inclination i , t_0 , surface brightness ratios for both datasets J_V , J_C^5 and ‘‘heat’’ parameters $h_{A,B}$ which take to account reflection effect for both components. After series of sets and trials we found out that code is unable to fit flat parts of minima, when whole CoRoT LC was used, thus we restrict our analysis only to eclipses from the time interval BJD=2454755.5:2454765.5 d (281 datapoints), which have less noise and shows clear flat minima with no signs of long-period variability, see Figure 1. The out-of eclipse regions were fitted using ASAS-SN LC, which is less affected by stellar pulsations, due to lower photometrical precision. Additionally we found that h_A parameter was always zero, thus we fix it to this value. This is possibly due to insufficient precision of ASAS-SN LC to get estimation of very weak reflection effect. To get uncertainties we sample the solution using EMCEE (Foreman-Mackey et al. 2013) with 50 walkers and 2000 iterations.

4 RESULTS

In the Figure 2 we show the best fit by multiple-epochs binary model for two epochs with large RV separation. We zoom into the wave-

Table 1. Spectral parameters from multiple-epoch fitting

Parameter	Star 1	Star 2
fit for RV_A		
γ , km s^{-1}	31.70 ± 0.10	
q	9.47 ± 0.05	
k_R	1.27 ± 0.02	
T_{eff} , K	7232 ± 3	5820 ± 8
fixed $\log(g)$, cgs	3.96	2.90
[Fe/H], dex	0.20 ± 0.01	
$V \sin i$, km s^{-1}	32 ± 1	41 ± 1
fit for RV_B		
γ , km s^{-1}	31.70 ± 0.10	
q	0.1056 ± 0.0005	
k_R	0.79 ± 0.01	
T_{eff} , K	5820 ± 8	7232 ± 3
fixed $\log(g)$, cgs	2.90	3.96
[Fe/H], dex	0.20 ± 0.01	
$V \sin i$, km s^{-1}	41 ± 1	32 ± 1

length range around the magnesium triplet, $H\alpha$ and in a 70 \AA interval in the red arm, where many double lines are clearly visible. We can see that the primary star ($T_{\text{eff}} = 7232 \text{ K}$, $\log(g) = 3.96$ cgs, [Fe/H] = 0.2 dex, $V \sin i = 32 \text{ km s}^{-1}$) contributes around 75% in the spectrum, while the secondary star ($T_{\text{eff}} = 5803 \text{ K}$, $\log(g) = 2.90$ cgs, [Fe/H] = 0.2 dex, $V \sin i = 40 \text{ km s}^{-1}$) and contributes to the remaining 25%. The derived mass ratio is $q \sim 0.11$ and systemic radial velocity $\gamma = 31.70 \text{ km s}^{-1}$. Additionally we make another multiple-epoch fit with another component’s RV finding same spectral parameters with inverted mass ratio $1/q = 9.47$. We present all spectroscopic results in the Table 1. The errors in the spectral parameters provided by `scipy.optimize.curve_fit` are nominal and largely underestimated. Based on simulations with synthetic spectra in Kovalev et al. (2022a, 2023), typical errors of multiple-epoch spectral analysis are $\Delta T_{\text{eff},A,B} \sim 240, 360 \text{ K}$, $\Delta \log(g)_{A,B} = 0.15, 0.20$ cgs, $\Delta[\text{Fe}/\text{H}] = 0.2$ dex, $\Delta V \sin i_{A,B} = 10, 30 \text{ km s}^{-1}$.

In Figure 3 we show the best fits of the CoRoT LC (top) and RV (bottom) by JKTEBOP, while zoomed version covering only eclipses can be found in Figure 4. The fit residuals (O-C) are typically small: ≤ 0.02 mag in total eclipse, ≤ 0.01 mag for LC in out eclipse regions (mostly due to high-frequency oscillations) and $\leq 4 \text{ km s}^{-1}$ for RVs. Only seven measurements for RV_B are off by $\geq 1 \text{ km s}^{-1}$ and they correspond to relatively low S/N spectra. The derived systemic velocities and mass ratio are similar to the values derived from a multiple-epoch spectral fit. Note $\gamma_A > \gamma_B$, as one will expect taking gravitational red shift into account, although this difference is well below uncertainties. We present results from JKTEBOP in the Table 2.

The oblateness of the components (0.0008, 0.0869) is small, but for secondary is larger than limit 0.04 (Popper & Etzel 1981), which can explain relatively big residuals at total eclipse, thus JKTEBOP solution should be improved by other code, for example ELLC.

There is another set of RV measurements from our spectra in Zhang et al. (2021), which we can use to check for possible systematic errors of our analysis. These RV were derived independently for blue and red arms of the spectrum. We only used values derived from blue arm of the spectra, because results for the red arm often are bad for a secondary component. Also we excluded RV values from spectra taken during eclipses, to be consistent with multiple-epoch measurements. The JKTEBOP results for these RVs are presented

⁵ ELLC have different definition of this parameter than other two codes.

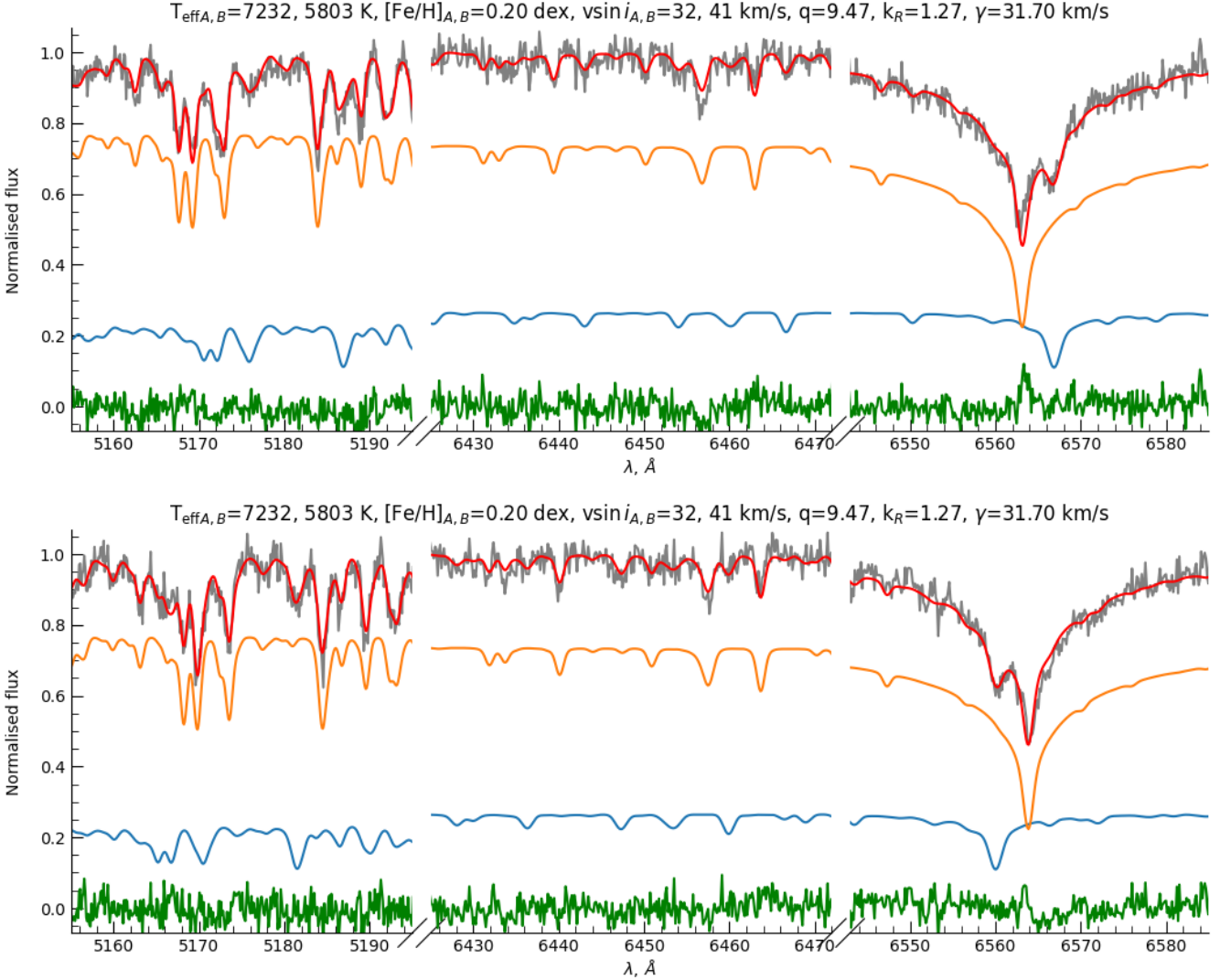


Figure 2. Example of the multiple-epoch fitting for spectra taken at MJD=58909.566 d (top) and MJD=58911.552 d (bottom). The observed spectrum is shown as a gray line, the best fit is shown as red line. The primary component is shown as the orange line, the secondary as a blue line. The fit residuals are shown as a green line.

in the right column of the Table 2. $K_{A,B}$ are slightly smaller than for multiple-epochs solution, which propagates into derived masses and sizes of components. The root mean square of residuals is smaller for RVs from simultaneous fit of multiple-epochs, thus we prefer them for further analysis.

Results derived by TLMC are collected in Table 3 and shown in Figure 5. They are consistent with JKTEBOP solution, although slightly different. Total eclipse is well fitted, while for secondary minimum residuals are symmetric relative to phase 0.5. These code was designed to fit exoplanet transits, so it can be expected to perform worse for stars. Anyway residuals are comparable to the amplitude of high-frequency pulsations. Out-of-eclipse part of LC is dominated by ellipsoidal variability ($\text{Ell}_{A,B}^{\max} \sim 0.25$, 6.0 per cent of total light) and reflection ($\text{Ref}_{A,B}^{\max} \sim 0.3$, 1.7 per cent of total light), while light beaming effect is negligible ($\text{Beam}_{A,B}^{\max} \sim 0.016$, 0.06 per cent of total light).

The results derived by ELLC are collected in Table 4. They are median values and standard deviations for all fitted parameters.

Corresponding solution is shown in Figure 6. As you can see this model fits eclipses in CoRoT LC very well, with typical residuals ≤ 0.01 mag. The primary eclipse in ASAS-SN LC also well fitted, although secondary eclipse is fitted poorly. This can be due to low precision and poor coverage of eclipses in ASAS-SN LC, although it can also indicate a long period variability of TV Mon, because ASAS-SN LC was observed ~ 2200 days later than CoRoT LC. If we compute fit residuals for CoRoT datapoints outside the time interval $\text{BJD}=2454755.5:2454756.5$ d, they are significantly larger - up to 0.03 mag during the total eclipse, while there is almost no difference for secondary minimum. This can indicate a slight long period variability of the secondary component (see Section 6), which is not included in our LC model. Resulting values of radii differ from previous solution: primary being slightly smaller $R_A = 2.43 R_{\odot}$ and secondary is slightly larger $R_B = 2.90 R_{\odot}$. Secondary radius is below the critical value: $R_B/a = 0.2020 < R_B^{\text{lim}}/a = 0.2869$. Inclination is almost the same as in previous solutions. Corner plot for fitted parameters can be found in Figure D1.

Table 2. JKTEBOP solutions using two RV datasets. Error's estimates are from MC simulations.

Parameter	CoRoT with multiple-epoch RV	CoRoT with Zhang et al. (2021) RV
fixed:		
Grav. darkening _A		0.32
Grav. darkening _B		0.32
Limb darkening A		0.3527, 0.2934
Limb darkening B		0.4548, 0.2264
$e \cos \omega$		0.0
$e \sin \omega$		0.0
fitted:		
J	0.2371±0.0010	0.2371±0.0009
$(R_A + R_B)/a$	0.3644±0.0017	0.3644±0.0018
R_B/R_A	1.1060±0.0022	1.1060±0.0022
i°	89.999±0.034	89.999±0.034
reflected light _A , mag	-0.003±0.004	-0.003±0.004
reflected light _B , mag	0.002±0.004	0.002±0.004
S_0 , mag	-0.022 ± 0.007	-0.022 ± 0.007
P , d	4.179741±0.000011	4.179729±0.000012
t_0 , BJD d	2454457.495664±0.000210	2454457.496574±0.000348
K_A , km s ⁻¹	16.62±0.05	15.76±0.32
K_B , km s ⁻¹	157.38±0.46	155.32±0.55
γ_A , km s ⁻¹	31.72±0.09	31.78±0.29
γ_B , km s ⁻¹	31.56±0.81	31.45±0.79
derived		
L_B/L_A	0.318±0.017	0.318±0.002
a , R_\odot	14.375±0.040	14.134±0.055
q	0.1056±0.0003	0.1015±0.0020
M_A , M_\odot	2.064±0.018	1.969±0.022
M_B , M_\odot	0.2179±0.0017	0.200±0.005
R_A , R_\odot	2.488±0.016	2.446±0.016
R_B , R_\odot	2.751±0.016	2.705±0.016
log (g) _A , cgs	3.961±0.005	3.955±0.005
log (g) _B , cgs	2.897±0.004	2.874±0.010
rms of the residuals:		
LC, mmag	5.230	5.302
RV _A , km s ⁻¹	0.171	1.378
RV _B , km s ⁻¹	1.629	1.287

4.1 Verification with WD

We use Wilson–Devinney method WD ([Wilson & Devinney 1971](#); [Wilson 1979](#)) with PYWD2015 ([Güzel & Özdarcın 2020](#)) user interface to verify ELLC solution. Same datasets were fitted by differential correction program with dimensionless potentials Ω , inclination, $T_{\text{eff}B}$, A_B as free parameters. Also bandpass luminosity L_1 of the primary component and third light were fitted for two LC. All other parameters were fixed. We show solution derived after 12 iterations in [Figure 7](#) and [Table 5](#). Residuals for eclipses are ≤ 5 mmag for CoRoT dataset, ASAS-SN V mostly have residuals ≤ 0.05 mag, with 0.1 mag residuals at primary eclipse. Solution is slightly different from ELLC, with secondary component being a bit smaller (~ 5 per cent). Also one can get good fit, only with non zero third light contribution.

5 SED FITTING

Spectral energy distribution (SED) can provide independent estimate of system's parameters. We use published photometry and try to utilise out-of-eclipse measurements, when it is possible. To

fit the SED we apply the SPEEDYFIT package⁶, which uses [Kurucz \(1979\)](#) models with a Markov chain Monte-Carlo approach to find the global minimum and determine the errors on the fit parameters. We set constraints on the solution using the Gaia DR3 ([Gaia Collaboration et al. 2022](#)) parallax $\varpi = 1.0654 \pm 0.0201$ mas, masses and radii from LC solution. Errors on the constraints are included as priors in the Bayesian fitting process and are thus propagated to the final results. A more detailed description of the fitting process is given in [Vos et al. \(2017\)](#). We show resulting fit in [Figure 8](#) and list parameters in [Table 6](#). T_{eff} values are slightly differ from spectroscopic ones, with secondary component being slightly cooler and primary hotter in SED fit. Our photometrical measurements were not corrected for observations during eclipses, except W1 and W2, which can cause such discrepancy, although other explanation is also possible.

⁶ <https://github.com/vosjo/speedyfit>

Table 3. TLCM solution. Error's estimates are from 25000 MC simulations.

Parameter	value
fixed:	
$T_{\text{eff}A}$, K	7232
$\sqrt{e} \cos \omega$	0.0
$\sqrt{e} \sin \omega$	0.0
P , d	4.179741
fitted:	
J	0.2281 ± 0.0003
a/R_A	5.776 ± 0.012
R_B/R_A	1.1027 ± 0.0024
Conjunction parameter b	0.000072 ± 0.014472
$u_{+,-} A$	$0.86 \pm 0.03, -0.59 \pm 0.12$
$u_{+,-} B$	$0.05 \pm 0.02, -1.01 \pm 0.08$
Albedo A	0.63 ± 0.14
Albedo B	0.66 ± 0.03
t_0 , BJD d	$2454457.49559 \pm 0.00006$
K_A , km s ⁻¹	16.634 ± 0.065
q	0.1057 ± 0.0004
γ , km s ⁻¹	31.68 ± 0.06
derived	
R_A/a	0.1731 ± 0.0004
$T_{\text{eff}B}$, K	5177 ± 2
i°	$89.999^{+0.007}_{-0.141}$
a , R_\odot	14.375 ± 0.076
M_A , M_\odot	2.063 ± 0.033
M_B , M_\odot	0.218 ± 0.003
R_A , R_\odot	2.486 ± 0.014
R_B , R_\odot	2.742 ± 0.017
$\log(g)_A$, cgs	3.953
$\log(g)_B$, cgs	2.893

Table 4. ELIC solution. Error's estimates are from median and standard deviations of EMCEE sampling.

Parameter	value
fixed:	
P , d	4.179741
$a \sin i$, R_\odot	14.375
q	0.1057
e	0.0
h_A	0.0
fitted:	
R_A/a	0.16898 ± 0.00009
R_B/a	0.20197 ± 0.00007
i°	89.36 ± 0.01
J_V	0.1878 ± 0.0021
J_C	0.1939 ± 0.0001
h_B	0.286 ± 0.003
t_0 , BJD d	$2454457.49567 \pm 0.00001$
derived	
a , R_\odot	14.375 ± 0.076
M_A , M_\odot	2.063 ± 0.033
M_B , M_\odot	0.218 ± 0.004
R_A , R_\odot	2.427 ± 0.014
R_B , R_\odot	2.901 ± 0.016
$\log(g)_A$, cgs	3.982 ± 0.002
$\log(g)_B$, cgs	2.851 ± 0.003

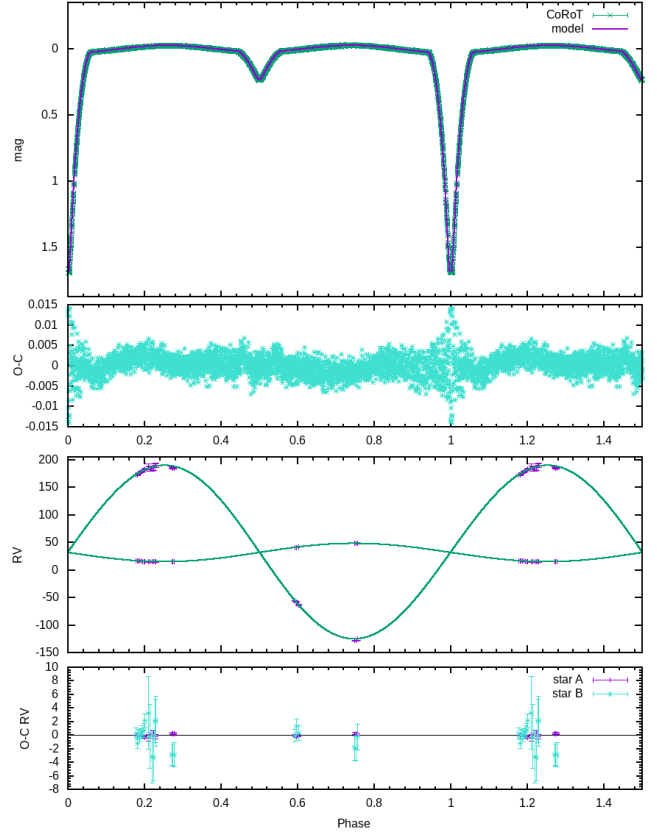


Figure 3. Phase-folded LC (top) and orbit (bottom) fits with JKTEBOP. The magnitudes are not calibrated.

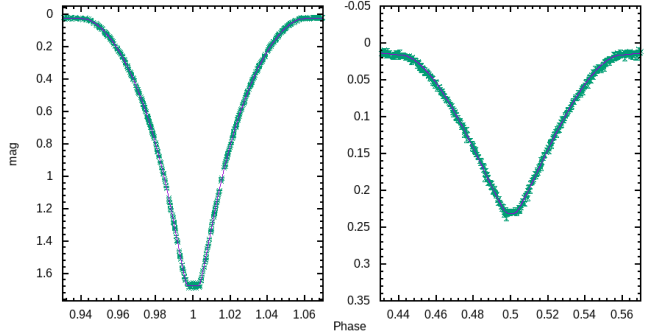


Figure 4. Same as Figure 3 for phases around eclipses.

6 PULSATIONS ANALYSIS

To explore pulsations in TV Mon we use different CoRoT photometry dataset “WHITEFLUXFIL”, available in the same datafile, which was not corrected for systematics, but has significantly more datapoints. These data have exposure time 32^s and contain 68103 datapoints with “STATUS” field equal to zero, which ensures that artefacts like “jumps” due to crossing of SAA by satellite were excluded. We normalise and flatten this LC by fitting a parabola to out-of-eclipse regions. Then we use a similar approach to [Chen et al. \(2021\)](#) analysis of OO Dra. As our LC model can not capture all possible variations of LC for all time interval, we computed averaged curve for the phase-folded LC and than subtract it from original LC. We use 301 phase bins, to ensure that each bin contains enough datapoints (typically 100-300). We show mean LC

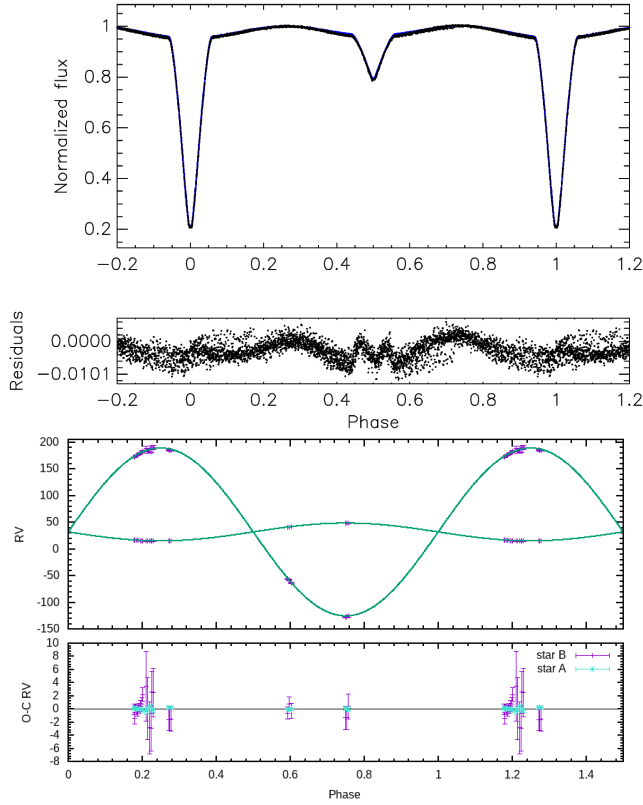


Figure 5. Phase-folded LC (top) and RV (bottom) fits with TLCM. Periodic structure is obvious in LC residuals around phase=0.5.

and eclipses from the start and end of the original LC in Figure 9. We see no pulsations in the primary eclipse, although it's flat part depth changes with time, which can indicate long period variability of secondary component, due to fast changing spots or some instrumental effect in CoRoT observations. Secondary eclipse show clear pulsations, with flat part of the minima having similar depth. Thus high-frequency pulsations come only from the primary component and LC data with phase from -0.06 till 0.06 were excluded from further analysis, leaving us with dataset of 60150 points.

We explore pulsations using PERIOD04 software (Lenz & Breger 2005). We follow steps described in Chen et al. (2021); Wang et al. (2023) to iteratively find frequencies in the range from 0 to 50 cycle per day (no strong peaks were found with larger frequencies), until residual Fourier spectrum have no peaks with $S/N > 4$. We identified 29 frequencies listed in Table 7 and shown in top panel of Figure 10, while the best fit pulsations model is shown in the bottom panel. None of the frequencies match to $f_{\text{sat}} = 1/P_{\text{sat}} = 86400^s/6182^s = 13.9715 \text{ day}^{-1}$ and it's multiples, where P_{sat} is the CoRoT satellite orbital period (Auvergne et al. 2009). Thus CoRoT team successfully removed artefacts, due to SAA crossing⁷. With frequency resolution of 0.055 day^{-18} we also searched for possible orbital harmonics ($f_i = Nf_{\text{orb}}$, $f_{\text{orb}} = 1/P = 0.239249 \pm 0.000001 \text{ day}^{-1}$) and combination frequencies. Unfortunately many peaks (i.e. f_1, f_3, f_5, f_9) are possibly originates from the imperfect removal of binarity-induced light variations, al-

⁷ As an exercise we computed Fourier spectrum for the raw "WHITEFLUX" minus mean LC. It shows two strong peaks with $f = f_{\text{sat}}, 4f_{\text{sat}}$.

⁸ it is quite low due to short timebase of CoRoT observations

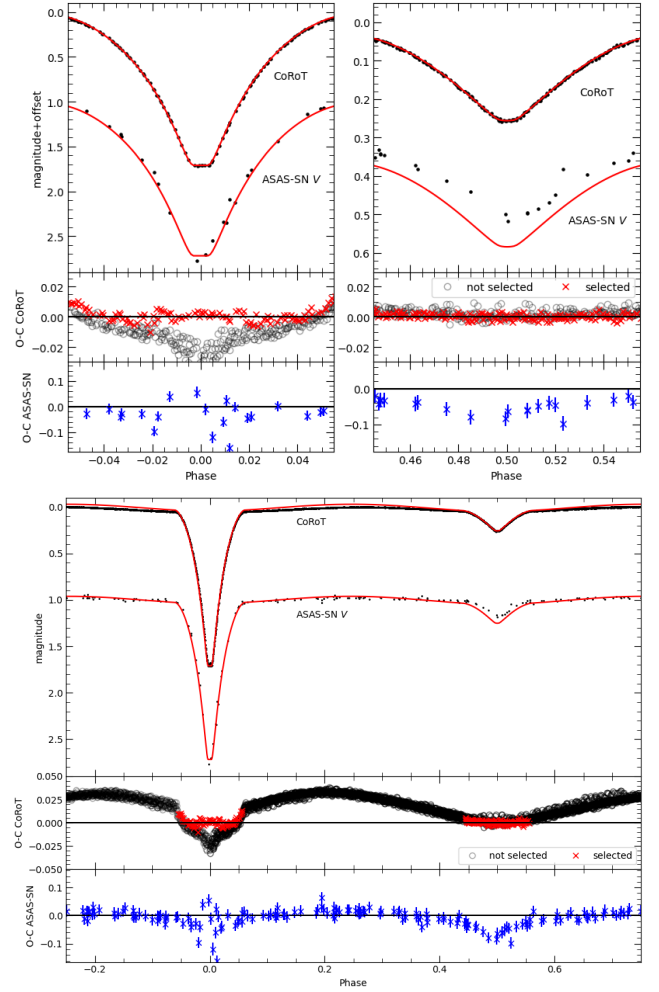


Figure 6. LC solution by ELLC code. We fit a whole ASAS-SN V dataset, but only a part of CoRoT data from eclipses in the time interval BJD=2454755.5:2454765.5 was used in fitting (top panels). Full LCs are shown in bottom panel, while the fit residuals are shown below each panel. For CoRoT data we also show residuals computed for datapoints, which were not used during fitting (gray/black open circles).

though some of them can be result of instrumental effects or long period variability of the secondary component. For example period value $P_{17} \sim 128 \text{ d}$, corresponding to f_{17} , is similar to the long period $P_{\text{long}} \sim 30P_{\text{orb}}$, detected in many Algol-type systems (Mennickent 2017). Only $f_2 = 23.57$, $f_4 = 27.53$, $f_6 = 20.87 \text{ day}^{-1}$ can be considered as independent frequencies, possibly δ Scuti pressure modes. Although f_5 is close to $115f_{\text{orb}}$, it has very strong peak in the Fourier spectrum and small error, which is enough to conclude, that it is just an accidental agreement. As Star A is likely to be a source of these pulsations, so we computed pulsation constants $Q = P_{\text{pul}}\sqrt{\rho/\rho_{\odot}}$, where P_{pul} is the pulsation period, ρ is a mean density of the star. We got $Q = 0.014, 0.016, 0.018 \text{ day}$ for f_4, f_2, f_6 respectively. We leave detailed physical modelling of these pulsations (see an example in Chen et al. (2021)) to the future studies.

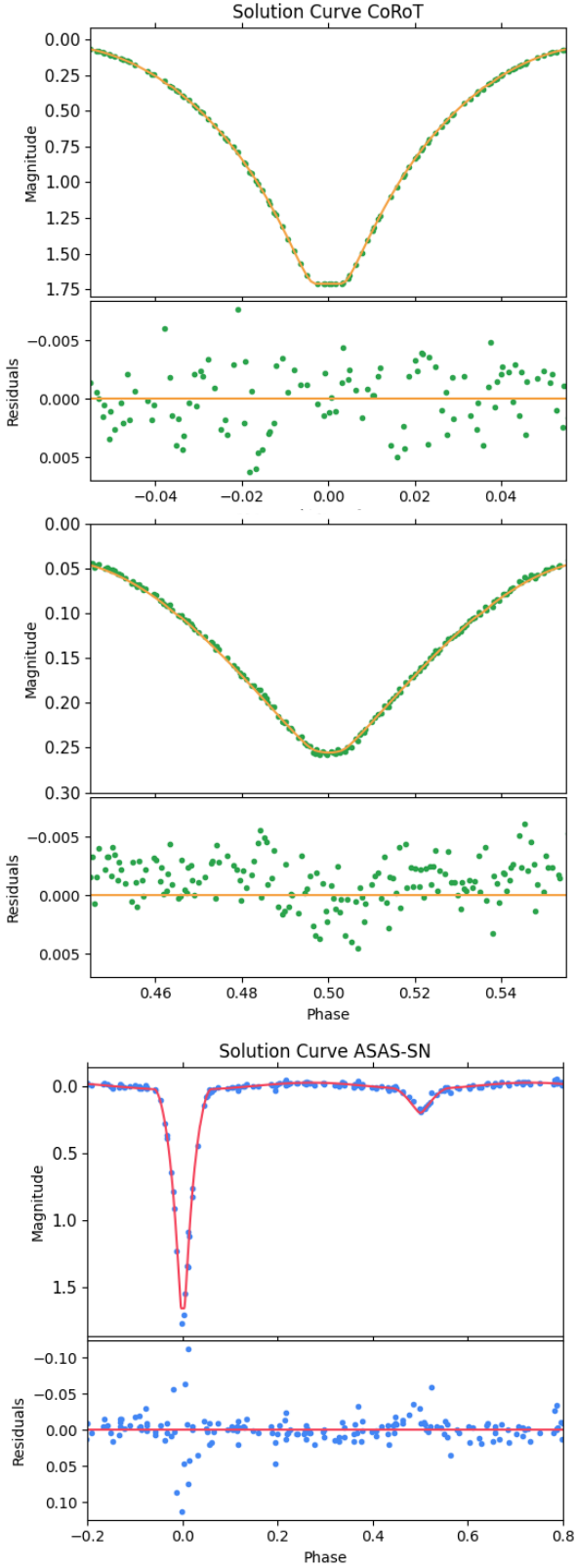


Figure 7. LC solution by WD using same data as ELLC code. Top panels show fit of the data, bottom panels show fit residuals.

Table 5. WD solution.

Parameter	value
fixed:	
P , d	4.179741
a , R_{\odot}	14.375
q	0.1057
e	0.0
A_A	1.0
$T_{\text{eff}A}$, K	7232
fitted:	
$T_{\text{eff}B}$, K	5059 ± 5
i°	89.45 ± 0.08
$L1_V$	9.503 ± 0.048
$L1_C$	9.274 ± 0.011
$L3_V$	0.057 ± 0.005
$L3_C$	0.025 ± 0.001
A_B	1.09 ± 0.03
Ω_A	6.051 ± 0.012
Ω_B	1.999 ± 0.001
derived	
r_1 (pole)	0.16817 ± 0.00033
r_1 (point)	0.16876 ± 0.00034
r_1 (side)	0.16862 ± 0.00034
r_1 (back)	0.16873 ± 0.00034
r_2 (pole)	0.18583 ± 0.00021
r_2 (point)	0.23558 ± 0.00071
r_2 (side)	0.19235 ± 0.00024
r_2 (back)	0.21692 ± 0.00040
R_A , R_{\odot}	2.423
R_B , R_{\odot}	2.852
$\log L_A$, L_{\odot}	1.158
$\log L_B$, L_{\odot}	0.678
$\log (g)_A$, cgs	3.98
$\log (g)_B$, cgs	2.87

7 DISCUSSION

7.1 System parameters

This is an Algol-like eclipsing binary system, which experienced mass transfer and mass-ratio reversal in the past. Massive primary component is hot, while much lighter secondary star is a cool red giant. Based on the absence of emission lines in $H\alpha$ region and secondary radius smaller than R_B^{lim} we can conclude that mass transfer is not active anymore.

Analysis of pulsations revealed three distinct frequencies of δ Scuti type associated with primary component. Several low frequencies pulsations, with larger amplitude were also identified, which can be interpreted as imperfect removal of binary flux variations or/and slow variability caused by spots. We checked VizieR for other CoRoT targets observed simultaneously with TV Mon and found five in $2'$ cone. Two of them belong to spectral type K3II and show irregular variability, while two others have same spectral type as TV Mon: A5IV and have stable LCs. Thus we think that slow variability is real and is not caused by some instrumental effect. Secondary component is a cool red giant, which can have magnetic activity, required to produce spots. As these spots seems to change very fast (see lower panel in Figure 10), we don't model them in our LC solutions.

We collect literature data for TV Mon in Table 8. Basically they agree with our estimations if we take uncertainties into account. For example *Gaia* DR3 Multiple Star Classifier solution, based

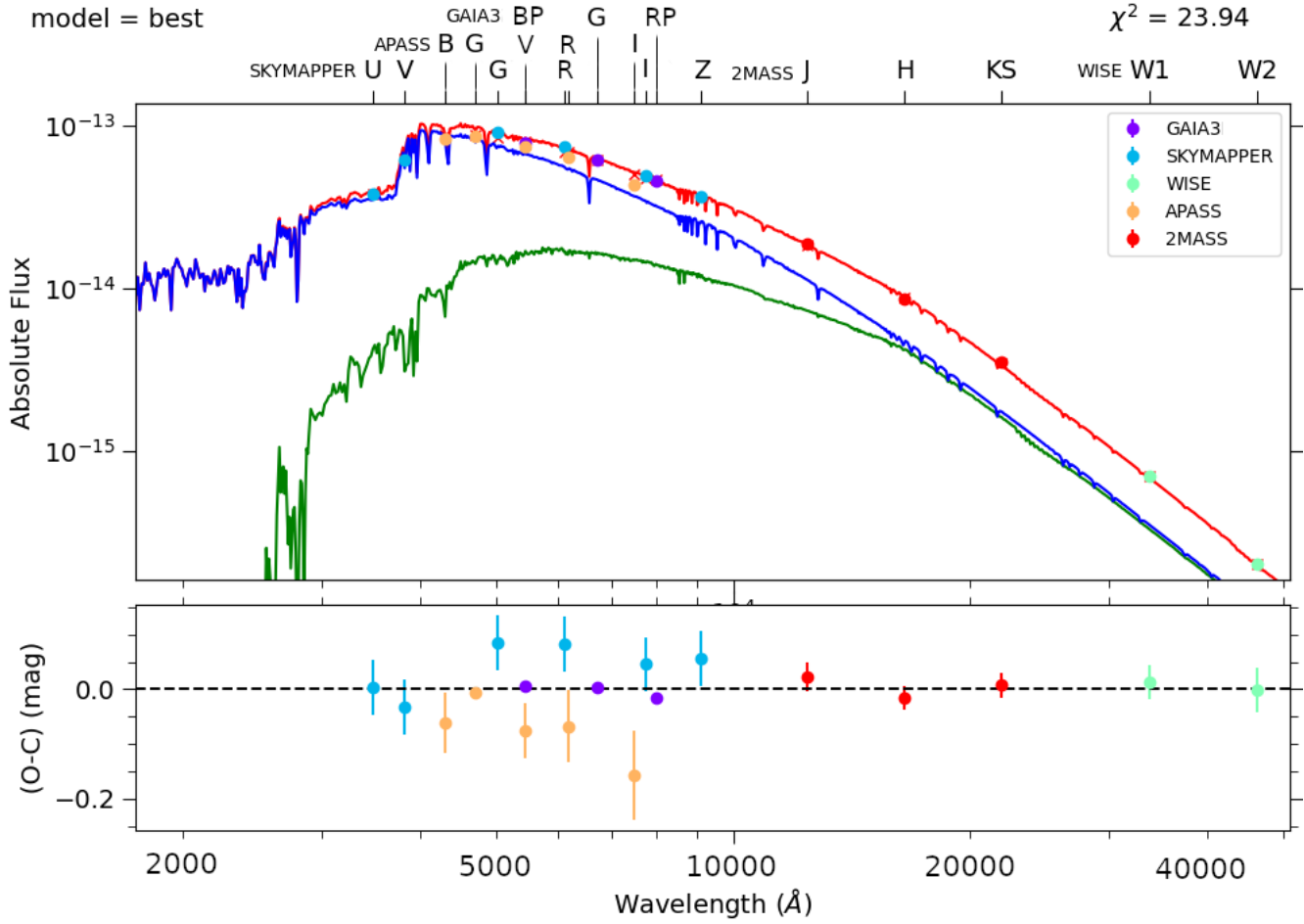


Figure 8. SED fitting with *SPEEDYFIT*. The top panels shows observations and spectral energy distribution of the system (red line), primary (blue line) and secondary (green line). The fit residuals are shown on the bottom panel.

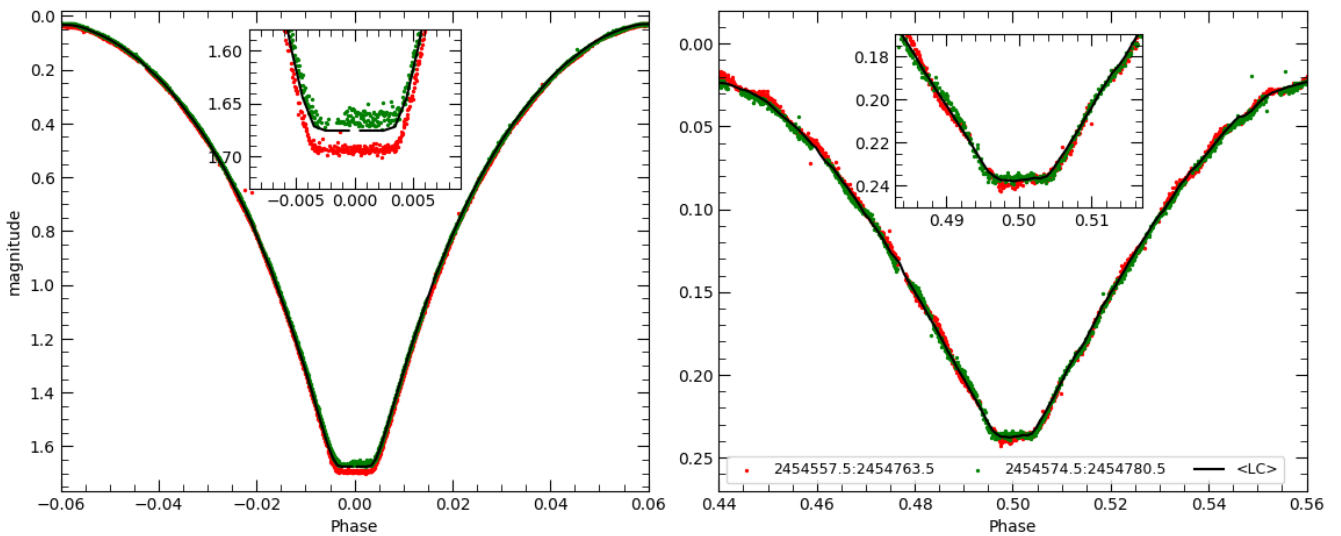


Figure 9. Mean LC and data for eclipses taken in the start and end parts of LC.

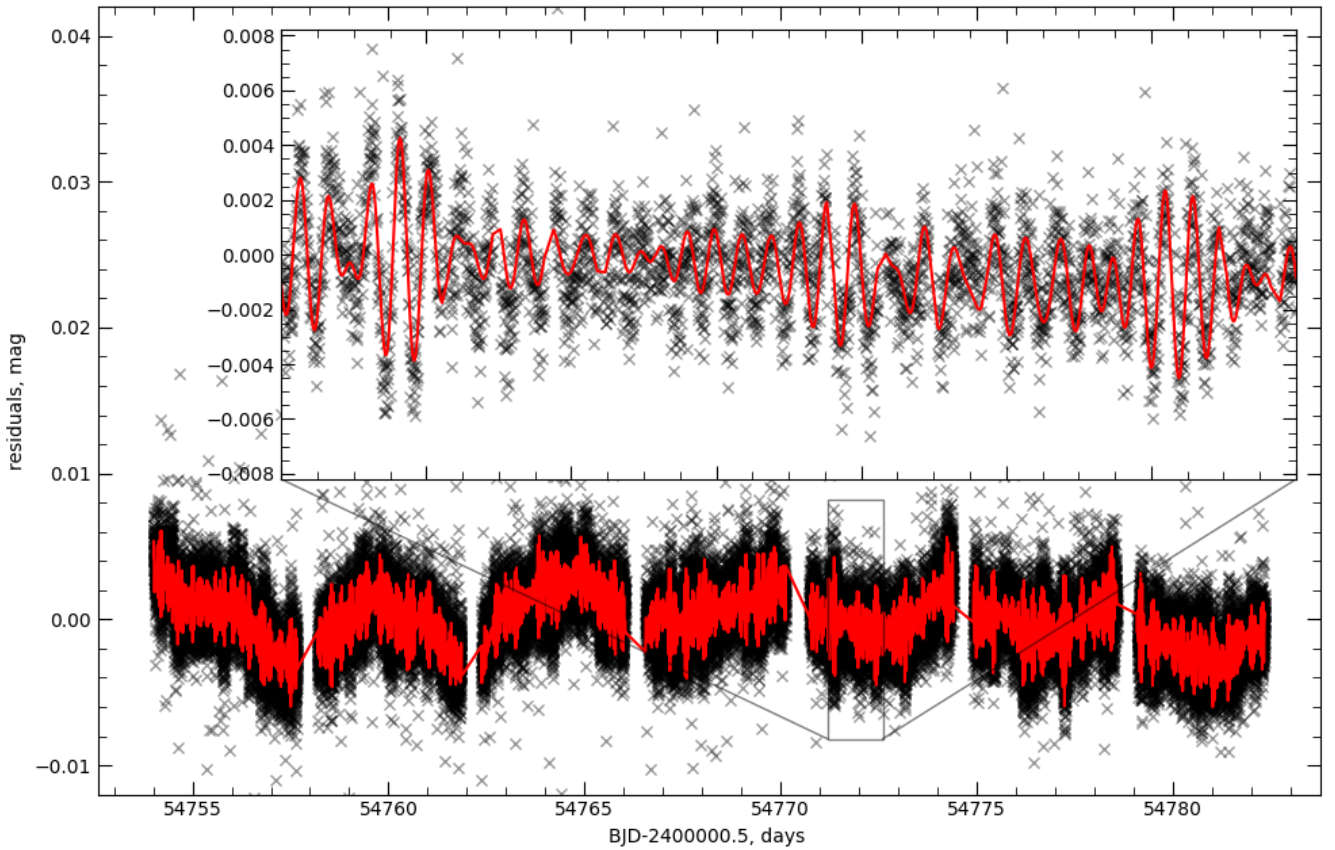
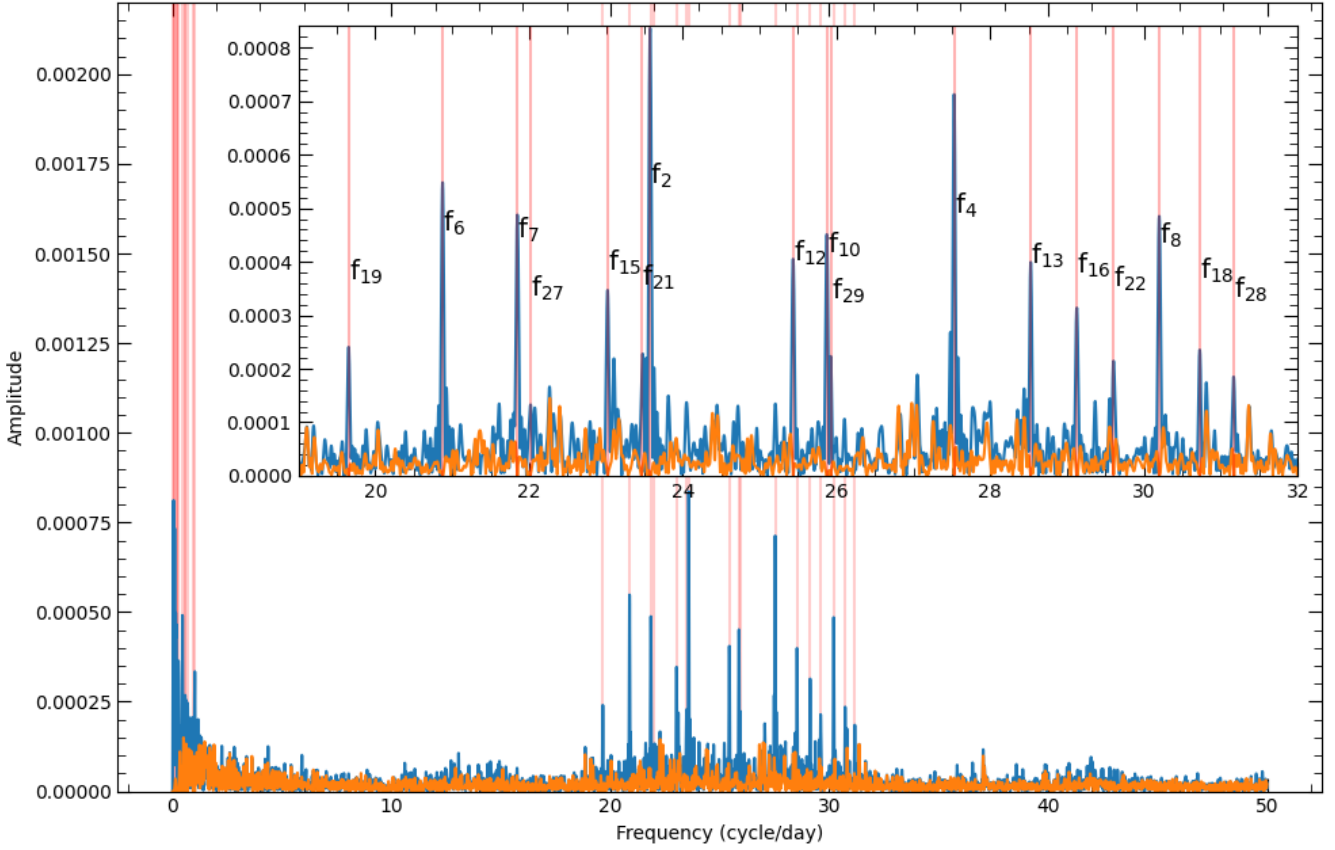


Figure 10. Fourier spectrum, with inline plot showing region with possible δ -Scuti pulsations (top) and best fit pulsation model (bottom). Vertical red lines indicates position of all identified frequencies. Orange line shows Fourier spectrum after removal of 29 frequencies.

Table 6. SED fitting results and observed photometry from Gaia DR3 [Gaia Collaboration et al. \(2022\)](#), APASS [Henden et al. \(2015\)](#), SKYMAPPER [Wolf et al. \(2018\)](#), 2MASS [Skrutskie et al. \(2006\)](#) and WISE [Cutri et al. \(2013\)](#). WISE values were computed as mean and standard deviation of out-of-eclipse parts of the time-series.

Observations (mag):	
GDR3 <i>G</i>	11.5146 ± 0.0032
GDR3 <i>BP</i>	11.7826 ± 0.0057
GDR3 <i>RP</i>	11.0990 ± 0.0086
APASS <i>B</i>	12.19 ± 0.06
APASS <i>V</i>	11.73 ± 0.05
APASS <i>G</i>	11.878 ± 0.006
APASS <i>R</i>	11.61 ± 0.07
APASS <i>I</i>	11.58 ± 0.08
SKYMAPPER <i>U</i>	13.41 ± 0.05
SKYMAPPER <i>V</i>	12.68 ± 0.05
SKYMAPPER <i>G</i>	11.71 ± 0.05
SKYMAPPER <i>R</i>	11.50 ± 0.05
SKYMAPPER <i>I</i>	11.42 ± 0.05
SKYMAPPER <i>Z</i>	11.38 ± 0.05
2MASS <i>J</i>	10.53 ± 0.03
2MASS <i>H</i>	10.31 ± 0.02
2MASS <i>K_s</i>	10.22 ± 0.02
WISE <i>W1</i>	10.1678 ± 0.0304
WISE <i>W2</i>	10.1983 ± 0.0409
Fitted parameters:	
<i>d</i> , pc	907^{+11}
$E(B - V)$, mag	$0.170^{+0.029}_{-0.027}$
$T_{\text{eff } A, B, K}$	$7624^{+194}_{-174}, 5187^{+130}_{-123}$

on very low resolution *BP, RP* spectra, have high goodness-of-fit score $\text{LOGPOSTERIOR}_{\text{MSC}}=329$ but very large uncertainties. This is possibly due to assumption of co-evolved binary, which is wrong for our system with mass transfer history.

Previous work by [Xiong et al. \(2023\)](#) used ASAS-SN photometry together with LAMOST-MRS RV from [Zhang et al. \(2021\)](#), while we utilise better photometry and updated RV, based on the same spectra. As we show in Section 4, systematic difference in RV will lead to slightly different stellar masses.

In the future red giant will become a low mass white dwarf (WD). Thus TV Mon will eventually become EL CVn type eclipsing binary system, like WASP 0346-21, which has similar mass ratio, but shorter period ([Lee et al. 2024](#)).

7.2 Binary evolution simulation

The low-mass component of TV Mon has a mass of $0.218 \pm 0.004M_{\odot}$, which is likely one type of envelope-stripped star, i.e. pre-ELM WD. The formation of (pre-)ELM WD binaries have been well studied in recent years (e.g., [Althaus et al. 2013](#); [Istrate et al. 2016](#); [Chen et al. 2017](#); [Sun & Arras 2018](#); [Li et al. 2019](#)). Following the work of [Li et al. \(2019\)](#), we try to construct the evolutionary history of TV Mon based on the observed parameters. The binary evolution simulations are performed via detailed stellar evolution code Modules for Experiments in Stellar Astrophysics (MESA, version 12115; [Paxton et al. 2011, 2013, 2015](#)). We adopt the Ledoux criterion and semi-convection mixing for the convection treatment, where the mixing length parameter is set to be 1.5, and semi-convection is modeled with an efficiency parameter of $\alpha_{\text{sc}} = 0.01$. We adopted the element abundances of Population I stars, i.e., metallicity $Z = 0.02$ and hydrogen mass fraction

$X = 0.70$. The mass transfer processes are simulated based on the Ritter scheme ([Ritter 1988](#)).

We first try to evolve both components simultaneously. Here we assumed that the binary would merge once the accretor fills its Roche lobe. The typical progenitors of pre-ELM WDs are generally in the range of $1.0 - 2.0M_{\odot}$ ([Li et al. 2019](#)). According to the total mass of TV Mon, i.e., $\sim 2.3M_{\odot}$, the progenitor of M_B should be larger than $1.15M_{\odot}$ (since the initial donor mass is larger than the initial accretor mass). For a given initial donor mass and the chosen accretion efficiency, one can approximately determine the initial accretor mass (initial mass ratio) according to the observational constraints on TV Mon. Then we test a series of binary models with varying initial binary parameters, i.e. donor mass, mass ratio, orbital period, accretion efficiency. Unfortunately, none of these models can reproduce the observation parameters of TV Mon. The binaries would either merge due to the Roche lobe overflow from the accretor or produce pre-ELM WDs massive than M_B . Therefore, in the subsequent simulations, we take the accretor as a mass point.

The accretion efficiency is a free parameter and cannot be limited in our simulations. As suggested by our previous work on Algol-type binary ([Kovalev et al. 2022a](#)), the accretion efficiency of 0.3 can support the observed parameters of TYC 2990-127-1 well. Therefore, our binary simulations adopt a fixed value of 0.3 for the accretion efficiency. Then the progenitor of M_B should be massive than $1.64M_{\odot}$. We test four groups of binary models with initial donor masses ranging from 1.7 to $2.1M_{\odot}$, the initial accretor masses and orbital separations adjust correspondingly to match the observations. The binary evolution results are shown in Figure 11. In the panel (a), we put the observed and simulated samples in the He WD mass-orbital period plane, where the theoretically fitted curve taken from [Lin et al. \(2011\)](#) is also shown for comparison. It is clear the He WD binaries produced from stable RLOF processes show a strong correlation between the orbital period and He WD mass. The observational parameters of TV Mon support such relation pretty well. In panel (b), we present the possible evolutionary history of TV Mon. The thick black line is for the binary evolution model and the thin grey lines are for single evolutionary tracks with masses from 1.7 to $2.1M_{\odot}$ (from right to the left), respectively. In our best model, the initial binary contains a $1.8M_{\odot}$ donor star and a $1.61M_{\odot}$ accretor, the initial orbital period is 0.626 d. The donor star fills its Roche lobe at the early MS stage, as shown in the red open circle. The donor then ascend RGB in the late mass transfer phase. The pre-ELM WD is born after the termination of mass transfer processes, as shown in the red open square. The pre-ELM WD would not enter into the cooling stage immediately because the residual hydrogen layer is still burning, sustaining a relatively high luminosity ([Istrate et al. 2014](#); [Chen et al. 2017](#); [Li et al. 2019](#)). The mass of the pre-ELM WD in panel (b) is $0.218M_{\odot}$, which coincides with the observations. The accretor mass after the mass transfer is $2.05M_{\odot}$. The detailed structure of the accretor is not considered in our simulations. According to the single stellar tracks (thin grey lines), we see that the inferred mass of M_A is in the range of $\sim 1.7 - 1.9M_{\odot}$, which is slightly lower than the observationally derived mass of M_A ($2.063 \pm 0.033M_{\odot}$). The discrepancy may originate from the fact that the accretor's rejuvenation process may alter the stellar structure comparing with the same mass single star (e.g. [Zhao et al. 2024](#); [Lau et al. 2024](#)). In panel (c), we present the masses of the two components as a function of evolutionary age. The onset and termination of the mass transfer processes are shown in red open circles and squares, respectively. The age of current state of TV Mon is approximately shown in grey dotted line. We see that the time elapsed since the end of mass transfer is about 250 Myr.

	Frequency cycles per day	Amplitude mmag	Phase rad/(2π)	comment
f_1	0.2107±0.0002	1.3773±0.0112	0.230±0.001	f_{orb}
f_2	23.5753±0.0002	0.8536±0.0089	0.617±0.002	δ Scuti
f_3	0.0605±0.0007	5.0481±0.1956	0.139±0.003	spot?
f_4	27.5301±0.0002	0.7048±0.0089	0.069±0.002	δ Scuti, 115 f_{orb}
f_5	0.0650±0.0006	4.7121±0.1950	0.933±0.003	f_3
f_6	20.8750±0.0003	0.5569±0.0089	0.042±0.003	δ Scuti
f_7	21.8481±0.0003	0.5057±0.0089	0.973±0.003	$f_6 + 4f_{\text{orb}}$
f_8	30.1983±0.0003	0.4897±0.0089	0.085±0.003	$f_4 + 11f_{\text{orb}}$
f_9	0.1717±0.0005	0.5670±0.0102	0.350±0.003	f_{orb}
f_{10}	25.8730±0.0005	0.4164±0.0091	0.300±0.003	$f_4 - 7f_{\text{orb}}$
f_{11}	0.2687±0.0004	0.5643±0.0100	0.991±0.003	$f_3 + f_{\text{orb}}$
f_{12}	25.4367±0.0004	0.4357±0.0089	0.725±0.003	$f_7 + 12f_{\text{orb}}$
f_{13}	28.5238±0.0004	0.3942±0.0089	0.478±0.004	$f_8 - 7f_{\text{orb}}$
f_{14}	0.4525±0.0005	0.4446±0.0099	0.293±0.004	$f_{11} + f_{\text{orb}}$
f_{15}	23.0240±0.0005	0.3680±0.0089	0.965±0.004	$f_6 + 9f_{\text{orb}}$
f_{16}	29.1255±0.0005	0.3385±0.0089	0.031±0.004	$f_2 + 23f_{\text{orb}}$
f_{17}	0.0078±0.0016	1.4647±0.1523	0.984±0.009	long period?
f_{18}	30.7261±0.0007	0.2420±0.0089	0.296±0.006	$f_{12} + 22f_{\text{orb}}$
f_{19}	19.6531±0.0007	0.2347±0.0088	0.101±0.006	$f_6 - 5f_{\text{orb}}$
f_{20}	0.5488±0.0020	0.2975±0.0354	0.692±0.014	$2f_{11}$
f_{21}	23.4627±0.0008	0.2291±0.0089	0.258±0.006	$f_2 - f_3$, side lobe?
f_{22}	29.6037±0.0007	0.2352±0.0089	0.157±0.006	$f_{14} + f_{16}$
f_{23}	0.5669±0.0018	0.3197±0.0359	0.032±0.013	f_{20} , side lobe?
f_{24}	0.6831±0.0008	0.2611±0.0096	0.384±0.006	$f_{14} + f_{\text{orb}}$
f_{25}	1.0127±0.0009	0.2021±0.0090	0.105±0.007	$f_3 + 4f_{\text{orb}}$
f_{26}	0.9351±0.0009	0.1933±0.0097	0.664±0.008	$f_{14} + 2f_{\text{orb}}$
f_{27}	22.0123±0.0011	0.1586±0.0089	0.338±0.009	$f_{21} - 6f_{\text{orb}}$
f_{28}	31.1712±0.0011	0.1518±0.0089	0.160±0.009	$f_{12} + 24f_{\text{orb}}$
f_{29}	25.9239±0.0012	0.1608±0.0092	0.113±0.009	f_{10} , side lobe

Table 7. Pulsation frequencies. Errors are from PERIOD04 based on Montgomery & O’Donoghue (1999).

Above all, our simulation could reproduce most of the important observed parameters of TV Mon. Our results suggest that TV Mon contains an envelope-stripped star born via binary interaction.

8 CONCLUSIONS

In this paper we use available observations to characterise dEB system TV Mon. Here we summarise our results:

- (i) we applied multiple-epochs spectral fitting to LAMOST-MRS data to derive RV and spectral parameters;
- (ii) we checked CoRoT LC and found high frequency pulsations of the primary component and signs of long period variability of the secondary component. The analysis of eclipses told us relative sizes of the stellar components and almost edge-on circular orbit;
- (iii) combined LC and RV solution provided us estimations for masses and radii of the components: $M_{A,B} = 2.063 \pm 0.033, 0.218 \pm 0.004 M_{\odot}$, $R_{A,B} = 2.427 \pm 0.014, 2.901 \pm 0.016 R_{\odot}$;
- (iv) SED analysis and Gaia parallax allowed us to get estimation of temperatures $T_{\text{eff},A,B} = 7624^{+194}_{-174}, 5184^{+130}_{-123}$ K and distance $d = 907 \pm 11$ pc.
- (v) we measured three δ Scuti type frequencies in primary component, while we also suspect TV Mon having a long period variability with period $P_{\text{long}} \sim 128$ days;
- (vi) this system experienced intensive mass transfer and mass ratio reversal in the past. Now it shows no signs of mass transfer in the spectra. The low mass component will shrink to the He WD, which mass and orbital period are in good agreement with

evolutionary models predictions. Eventually it will be EL CVn type eclipsing binary system.

TV Mon is a very interesting laboratory to study post-mass transfer binary systems. It will benefit from future observations like a high resolution spectroscopy and space based photometry. Relatively long (40 min) total eclipse phase allows to get detailed spectra of the red giant component. One definitely will take to account gravitational red shift and possibly convectional blue shift effects, when new spectra will be available. Longer photometrical time series will make possible more detailed analysis of δ Scuti pulsations in the primary and confirmation of possible long period variability of the secondary.

ACKNOWLEDGEMENTS

We thank Hans-Ludwig (LSW) for useful discussions. Guoshoujing Telescope (the Large Sky Area Multi-Object Fiber Spectroscopic Telescope LAMOST) is a National Major Scientific Project built by the Chinese Academy of Sciences. Funding for the project has been provided by the National Development and Reform Commission. LAMOST is operated and managed by the National Astronomical Observatories, Chinese Academy of Sciences. This work is supported by the National Key R&D Program of China (grant Nos. 2021YFA1600403, 2021YFA1600400), the Natural Science Foundation of China (grant Nos. 12125303, 12288102, 12090040/3, 12473034, 12103086, 12273105, 11703081, 11422324, 12073070), Yunnan Fundamental Research Projects (Nos. 202401BC070007

Table 8. Literature data compilation from Svechnikov & Kuznetsova (1990), Avvakumova et al. (2013), Hubscher et al. (2009), ASAS-SN Jayasinghe et al. (2018), Gaia DR3 FLAME and Multiple Star Classifier (MSC) Gaia Collaboration et al. (2022) and Xiong et al. (2023). Gaia DR3 values provided with 16 and 84 percentiles. (*) assuming single star.

Parameter	Value	reference
P , d	4.179742	Svechnikov
i°	87.5	Svechnikov
a , R_\odot	14.50	Svechnikov
q	0.15	Svechnikov
$R_{A,B}$, R_\odot	2.0, 3.2	Svechnikov
$M_{A,B}$, M_\odot	2.05, 0.3	Svechnikov
P , d	4.179742	Kreiner (2004)
P , d	4.1797418594	Avvakumova
t_0 , (HJD) d	2454457.4942	Hubscher
P , d	4.1797391	ASAS-SN
t_0 , (HJD) d	2457700.99512	ASAS-SN
d , pc	1179 ¹⁵¹² ₁₀	GDR3 MSC
A_G , mag	0.68 ^{0.94} ₀	GDR3 MSC
[Fe/H], dex	0.34 ^{0.50} _{-1.00}	GDR3 MSC
$T_{\text{eff}A,B}$, K	6857 ⁸⁰⁰⁰ ₆₀₇₈ , 5983 ⁷⁵³⁴ ₄₂₇₅	GDR3 MSC
$\log(g)_{A,B}$, cgs	3.59 ^{3.20} _{3.24} , 3.65 ^{4.40} _{3.30}	GDR3 MSC
$T_{\text{eff}A,B}$, K	7531 ± 136, 5023 ± 107	Xiong
$\log(g)_{A,B}$, cgs	4.10 ± 0.21, 2.84 ± 0.02	Xiong
[Fe/H] _{A,B} , dex	0.24 ± 0.13	Xiong
$M_{A,B}$, M_\odot	2.024 ± 0.040, 0.21 ± 0.04	Xiong
$R_{A,B}$, R_\odot	2.357 ± 0.187, 2.869 ± 0.151	Xiong
q	0.103 ± 0.022	Xiong
age t , Gyr	0.989 ^{1.122} _{0.863}	GDR3 FLAME*

and 202201BC070003), the Yunnan Revitalization Talent Support Program–Science & Technology Champion Project (No. 202305AB350003), the Key Research Program of Frontier Sciences of CAS (No. ZDBS-LY-7005), Yunnan Fundamental Research Projects (grant Nos. 202301AT070314, 202101AU070276, 202101AV070001), and the International Centre of Supernovae, Yunnan Key Laboratory (No. 202302AN360001). We also acknowledge the science research grant from the China Manned Space Project with Nos. CMS-CSST-2021-A10 and CMS-CSST-2021-A08. The authors gratefully acknowledge the “PHOENIX Supercomputing Platform” jointly operated by the Binary Population Synthesis Group and the Stellar Astrophysics Group at Yunnan Observatories, Chinese Academy of Sciences. This research has made use of NASA’s Astrophysics Data System, the SIMBAD data base, and the VizieR catalogue access tool, operated at CDS, Strasbourg, France. It also made use of TOPCAT, an interactive graphical viewer and editor for tabular data (Taylor 2005). *Gaia* (<https://www.cosmos.esa.int/gaia>), processed by the *Gaia* Data Processing and Analysis Consortium (DPAC, <https://www.cosmos.esa.int/web/gaia/dpac/consortium>). Funding for the DPAC has been provided by national institutions, in particular the institutions participating in the *Gaia* Multilateral Agreement. This research has made use of the NASA/IPAC Infrared Science Archive, which is funded by the National Aeronautics and Space Administration and operated by the California Institute of Technology.

DATA AVAILABILITY

The data underlying this article will be shared on reasonable request to the corresponding author.

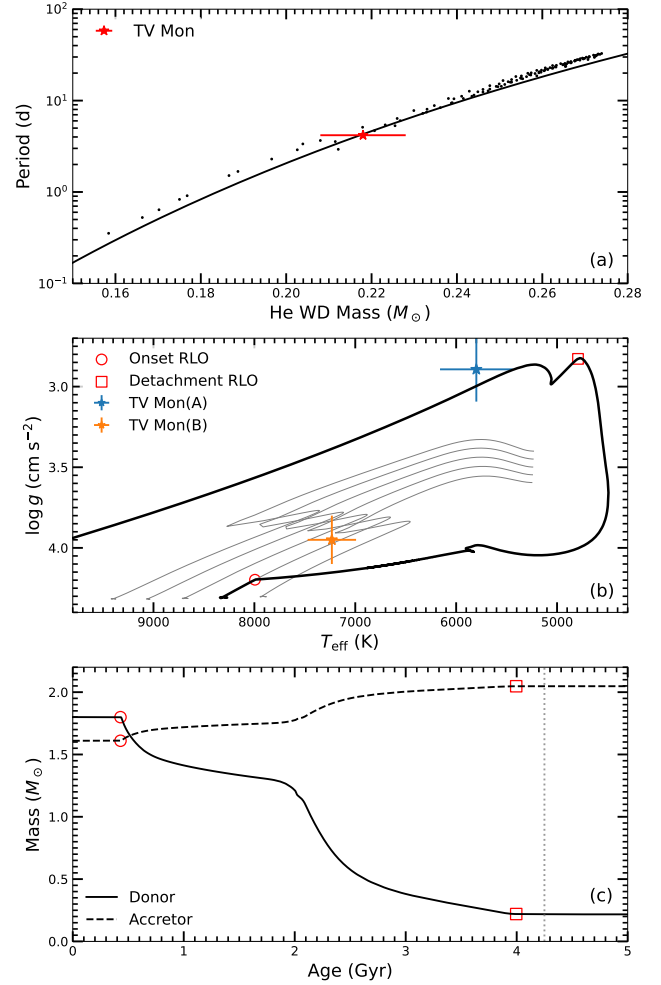


Figure 11. The evolutionary models of TV Mon. Panel (a): The WD mass-orbital period plane in the simulations. The black solid line is for the theoretically fitted curve of Lin et al. (2011). Panel (b): The evolutionary track in $T_{\text{eff}} - \log g$ plane for the best model. The black solid line is for the donor in the binary evolution and the grey lines are for the single evolution tracks with masses from 1.7 to 2.1 M_\odot , from right to left. The observed parameters for the two components of TV Mon are shown in colored stars. The onset and detachment of Roche lobe overflow (RLO) are shown in red open circle and square, respectively. Panel (c): The masses of the two components as a function of the evolutionary age. The grey dotted line is the approximate age in the current state of TV Mon according to the results in panel (a).

REFERENCES

- Althaus L. G., Miller Bertolami M. M., Córscico A. H., 2013, *A&A*, **557**, A19
- Auvergne M., et al., 2009, *A&A*, **506**, 411
- Avvakumova E. A., Malkov O. Y., Kniazev A. Y., 2013, *Astronomische Nachrichten*, **334**, 860
- Barge P., Baglin A., Auvergne M., CoRoT Team 2008, in Sun Y.-S., Ferraz-Mello S., Zhou J.-L., eds, Proceedings of the International Astronomical Union Vol. 249, Exoplanets: Detection, Formation and Dynamics. pp 3–16, doi:10.1017/S1743921308016293
- COROT Team 2016, VizieR Online Data Catalog: CoRoT observation log (N2-4.4) (CoRoT 2016), VizieR On-line Data Catalog: B/corot. Originally published in: CoRoT Data Center (2014)
- Chen X., Maxted P. F. L., Li J., Han Z., 2017, *MNRAS*, **467**, 1874
- Chen X., Zhang X., Li Y., Chen H., Luo C., Su J., Chen X., Han Z., 2020,

- ApJ, 895, 136
- Chen X., Zhang X., Li Y., Luo C., Li X., Su J., Chen X., 2021, ApJ, 920, 76
- Csizmadia S., 2020, MNRAS, 496, 4442
- Cui X.-Q., et al., 2012, Research in Astronomy and Astrophysics, 12, 1197
- Cutri R. M., et al., 2013, Explanatory Supplement to the AllWISE Data Release Products, Explanatory Supplement to the AllWISE Data Release Products, by R. M. Cutri et al.
- Czesla S., Schröter S., Schneider C. P., Huber K. F., Pfeifer F., Andreasen D. T., Zechmeister M., 2019, PyA: Python astronomy-related packages (ascl:1906.010)
- El-Badry K., 2022, Research Notes of the American Astronomical Society, 6, 137
- Foreman-Mackey D., 2016, The Journal of Open Source Software, 1, 24
- Foreman-Mackey D., Hogg D. W., Lang D., Goodman J., 2013, PASP, 125, 306
- Gaia Collaboration et al., 2022, arXiv e-prints, p. arXiv:2208.00211
- Grupp F., 2004a, A&A, 420, 289
- Grupp F., 2004b, A&A, 426, 309
- Güzel O., Özdarcan O., 2020, Contributions of the Astronomical Observatory Skalnaté Pleso, 50, 535
- Han Z.-W., Ge H.-W., Chen X.-F., Chen H.-L., 2020, Research in Astronomy and Astrophysics, 20, 161
- Henden A. A., Levine S., Terrell D., Welch D. L., 2015, in American Astronomical Society Meeting Abstracts #225. p. 336.16
- Hubscher J., Steinbach H.-M., Walter F., 2009, Information Bulletin on Variable Stars, 5889, 1
- Istrate A. G., Tauris T. M., Langer N., Antoniadis J., 2014, A&A, 571, L3
- Istrate A. G., Marchant P., Tauris T. M., Langer N., Stancliffe R. J., Grassitelli L., 2016, A&A, 595, A35
- Jayasinghe T., et al., 2018, MNRAS, 477, 3145
- Kovalev M., 2019, PhD thesis, Heidelberg University, doi:10.11588/heidok.00027411
- Kovalev M., Bergemann M., Ting Y.-S., Rix H.-W., 2019, A&A, 628, A54
- Kovalev M., Li Z., Zhang X., Li J., Chen X., Han Z., 2022a, MNRAS, 513, 4295
- Kovalev M., Chen X., Han Z., 2022b, MNRAS, 517, 356
- Kovalev M., Wang S., Chen X., Han Z., 2023, MNRAS, 519, 5454
- Kovalev M., Zhou Z., Chen X., Han Z., 2024, MNRAS, 527, 521
- Kreiner J. M., 2004, Acta Astron., 54, 207
- Kurucz R. L., 1979, ApJS, 40, 1
- Lau M. Y. M., Hirai R., Mandel I., Tout C. A., 2024, ApJ, 966, L7
- Lee J. W., Hong K., Jeong M.-J., Wolf M., 2024, arXiv e-prints, p. arXiv:2407.17729
- Lenz P., Breger M., 2005, Communications in Asteroseismology, 146, 53
- Li Z., Chen X., Chen H.-L., Han Z., 2019, ApJ, 871, 148
- Lin J., Rappaport S., Podsiadlowski P., Nelson L., Paxton B., Todorov P., 2011, ApJ, 732, 70
- Maxted P. F. L., 2016, A&A, 591, A111
- McLaughlin D. B., 1924, ApJ, 60, 22
- Mennickent R. E., 2017, Serbian Astronomical Journal, 194, 1
- Montgomery M. H., O'Donoghue D., 1999, Delta Scuti Star Newsletter, 13, 28
- Paxton B., Bildsten L., Dotter A., Herwig F., Lesaffre P., Timmes F., 2011, ApJS, 192, 3
- Paxton B., et al., 2013, ApJS, 208, 4
- Paxton B., et al., 2015, ApJS, 220, 15
- Popper D. M., Etzel P. B., 1981, AJ, 86, 102
- Ricker G. R., et al., 2015, Journal of Astronomical Telescopes, Instruments, and Systems, 1, 014003
- Ritter H., 1988, A&A, 202, 93
- Rossiter R. A., 1924, ApJ, 60, 15
- Skrutskie M. F., et al., 2006, AJ, 131, 1163
- Sokolovsky K., Maceroni C., Hareter M., Damiani C., Balaguer-Núñez L., Ribas I., 2010, Communications in Asteroseismology, 161, 55
- Southworth J., 2013, A&A, 557, A119
- Sun M., Arras P., 2018, ApJ, 858, 14
- Svechnikov M., Kuznetsova E., 1990, VizieR Online Data Catalogue
- Taylor M. B., 2005, in Shopbell P., Britton M., Ebert R., eds, Astronomical Society of the Pacific Conference Series Vol. 347, Astronomical Data Analysis Software and Systems XIV. p. 29
- Torres G., Andersen J., Giménez A., 2010, A&ARv, 18, 67
- Tsevech V. P., 1980, Peremennye zvezdy i ikh nabliudenie. Moskva, Nauka
- Vos J., Østensen R. H., Vučković M., Van Winckel H., 2017, A&A, 605, A109
- Wang K., Ren A., Andersen M. F., Grundahl F., Chen T., Pallé P. L., 2023, AJ, 166, 42
- Wilson R. E., 1979, ApJ, 234, 1054
- Wilson R. E., Devinney E. J., 1971, ApJ, 166, 605
- Wolf C., et al., 2018, Publ. Astron. Soc. Australia, 35, e010
- Xiong J., et al., 2023, AJ, 165, 30
- Zhang B., et al., 2021, ApJS, 256, 14
- Zhao G., Zhao Y.-H., Chu Y.-Q., Jing Y.-P., Deng L.-C., 2012, Research in Astronomy and Astrophysics, 12, 723
- Zhao Z.-Q., Li Z.-W., Xiao L., Ge H.-W., Han Z.-W., 2024, MNRAS, 531, L45

APPENDIX A: SPECTRAL MODELS

The synthetic spectra are generated using NLTE MPIA online-interface <https://nlte.mpia.de> (see Chapter 4 in Kovalev 2019) on wavelength intervals 4870:5430 Å for the blue arm and 6200:6900 Å for the red arm with spectral resolution $R = 7500$. We use NLTE (non-local thermodynamic equilibrium) spectral synthesis for H, Mg I, Si I, Ca I, Ti I, Fe I and Fe II lines (see Chapter 4 in Kovalev 2019, for references).

The grid of models (6200 in total) is computed for points randomly selected in a range of T_{eff} between 4600 and 8800 K, $\log(g)$ between 1.0 and 4.8 (cgs units), $V \sin i$ from 1 to 300 km s^{-1} and $[\text{Fe}/\text{H}]^9$ between -0.9 and $+0.9$ dex. The model is computed only if linear interpolation of the MAFAGS-OS(Grupp 2004a,b) stellar atmosphere is possible for a given point in parameter space. Microturbulence is fixed to $V_{\text{mic}} = 2 \text{ km s}^{-1}$ for all models.

APPENDIX B: WISE LIGHT CURVES

We show WISE light curves in Figure B1. Eclipses (parts between black vertical lines) were excluded, when we recompute photometry for SED fitting.

APPENDIX C: RV MEASUREMENTS

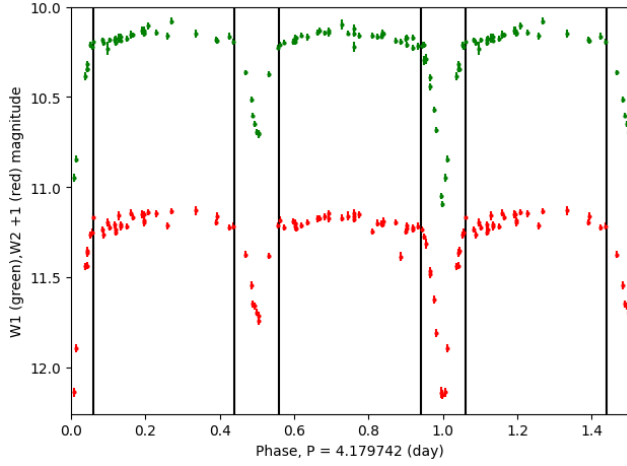
We provide RV measurements from the multiple-epoch fit in Table C1.

APPENDIX D: EMCEE SAMPLE OF ELLC SOLUTION

In Figure D1 we show corner plot (Foreman-Mackey 2016) with EMCEE sampling results for ELLC solution. There is strong correlation between R_A and R_B and weaker correlation between J_C and i .

This paper has been typeset from a $\text{\TeX}/\text{\LaTeX}$ file prepared by the author.

⁹ We used $[\text{Fe}/\text{H}]$ as a proxy of overall metallicity, abundances for all elements are scaled with Fe.

**Figure B1.** WISE light curves.**Table C1.** Radial velocity measurements. Errors we adjusted by JKTEBOP to reach unity in reduced χ^2 . We subtract 2400000.5 days from time values.

BJD d	RV_A km s^{-1}	RV_B km s^{-1}	phase
58530.5432	40.93 ± 0.16	-55.73 ± 0.90	0.593
58530.5599	41.13 ± 0.17	-57.64 ± 1.05	0.597
58530.5828	41.70 ± 0.17	-63.03 ± 1.10	0.606
58850.6423	16.83 ± 0.10	172.54 ± 0.79	0.176
58850.6562	16.82 ± 0.10	172.60 ± 0.82	0.180
58850.6687	16.55 ± 0.10	175.15 ± 0.75	0.183
58850.6882	16.38 ± 0.11	176.79 ± 0.77	0.187
58850.7014	16.22 ± 0.10	178.30 ± 0.75	0.191
58850.7139	16.06 ± 0.11	179.75 ± 0.88	0.194
58850.7319	15.89 ± 0.11	181.41 ± 1.01	0.198
58850.7444	15.63 ± 0.11	183.82 ± 1.01	0.201
58909.5526	15.40 ± 0.16	186.05 ± 1.56	0.271
58909.5658	15.44 ± 0.16	185.62 ± 1.65	0.274
58909.5789	15.49 ± 0.17	185.20 ± 1.78	0.277
58911.5517	48.45 ± 0.24	-126.91 ± 1.78	0.749
58911.5649	48.45 ± 0.24	-126.92 ± 1.82	0.752
58911.5774	48.26 ± 0.26	-125.12 ± 1.91	0.755
58913.4793	15.24 ± 0.44	187.62 ± 5.32	0.210
58913.4918	15.52 ± 0.40	184.90 ± 4.73	0.213
58913.5147	15.71 ± 0.33	183.13 ± 3.91	0.219
58913.5328	15.63 ± 0.30	183.83 ± 3.41	0.223
58913.5453	15.00 ± 0.27	183.83 ± 3.19	0.226
58913.5585	14.97 ± 0.31	190.22 ± 3.69	0.229

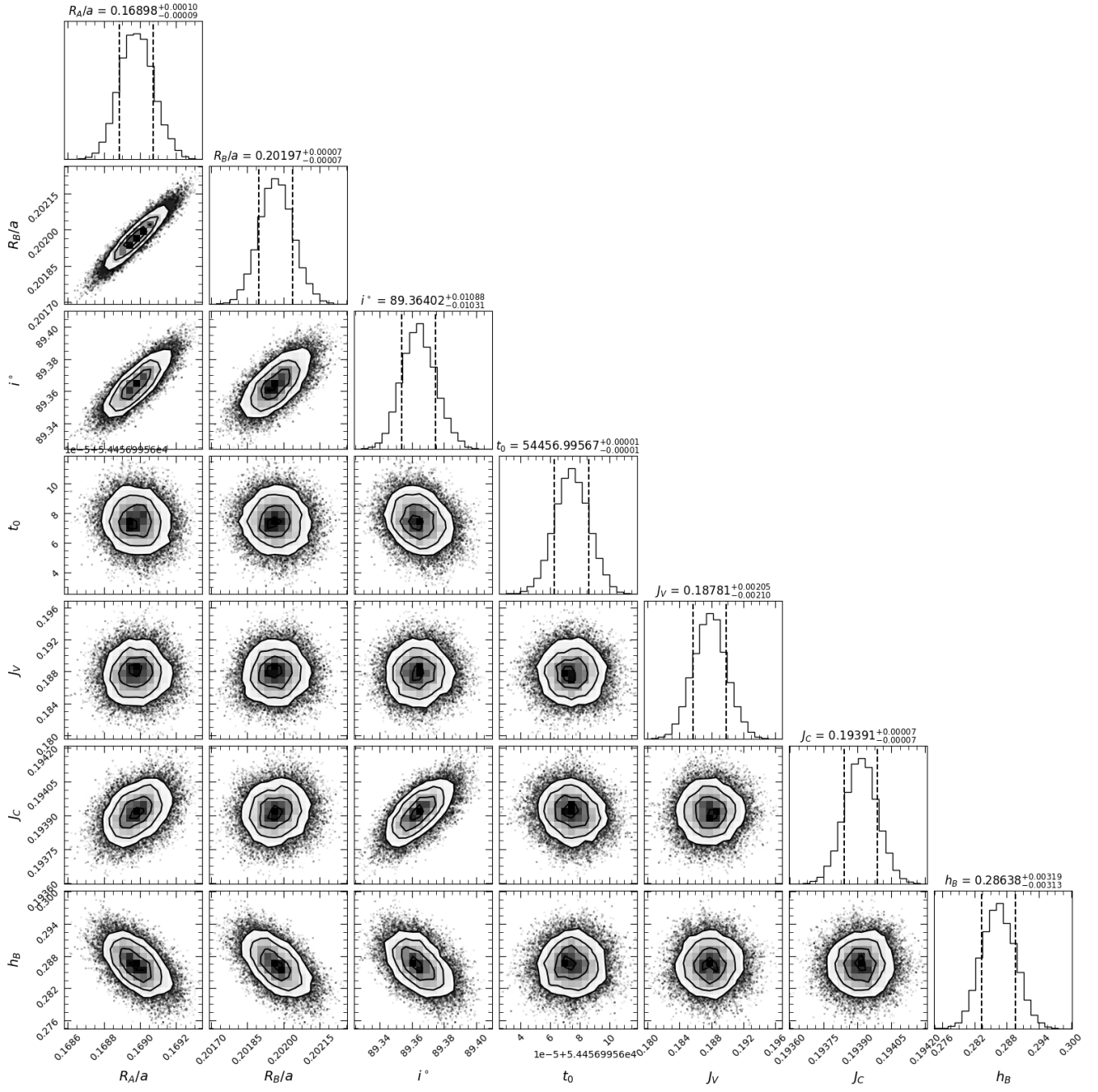


Figure D1. Corner plot for the sampling of ELIC solution. Titles show 16, 50 and 84 percentiles.